PCCP

ROYAL SOCIETY OF CHEMISTRY

PAPER

View Article Online
View Journal | View Issue

Cite this: *Phys. Chem. Chem. Phys.*, 2024, **26**, 13814

Modelling bulk and surface characteristics of cubic CeO_2, Gd_2O_3, and gadolinium-doped ceria using a partial charge framework†

Josef M. Gallmetzer, Jakob Gamper, Felix R. S. Purtscher and Thomas S. Hofer *

The development and characterization of materials for solid oxide fuel cells (SOFC) is an important step towards sustainable energy technologies. This present study models cubic CeO_2, Gd_2O_3, and gadolinium-doped ceria (GDC) using newly constructed interaction potentials based on a partial atom charge framework. The interaction model was validated by comparing the structural properties with experimental reference data, which were found to be in good agreement. Validation of the potential model was conducted considering the surface stability of CeO_2 and Gd_2O_3. Additionally, the accuracy of the novel potential model was assessed by comparing the oxygen diffusion coefficient in GDC*n* (*n* = 4–15) and the associated activation energy. The results demonstrate that the novel potential model is capable of describing the oxygen diffusion in GDC. In addition, this study compares the vibrational properties of the bulk with density functional theory (DFT) calculations, using a harmonic frequency analysis that avoids the need for computationally expensive quantum mechanical molecular dynamics (QM MD) simulations. The potential is compatible with a reactive water model, thus providing a framework for the simulation of solid–liquid interfaces.

Received 17th October 2023,
Accepted 5th April 2024

DOI: 10.1039/d3cp05053j

rsc.li/pccp

1 Introduction

Although significant advances in science and technology have been achieved during the last century, meeting the growing global demand for energy represents a continuously increasing challenge of the new millennium.[1] The quest for alternative energy sources has emerged as an increasingly active research area, which is directly linked to concerns over accelerated climate change.[2] One promising method for creating sustainable and environmentally friendly energy systems in the heavy transportation industry, particularly in heavy-duty transport[3] and aviation,[4] utilizes fuel cell (FC) technology. FCs directly convert chemical energy into usable electricity.[5] Various implementations, such as proton-exchange membrane FCs,[6] phosphoric and solid acid FCs,[7] or alkaline FCs,[8] have been developed. Solid oxide fuel cells (SOFCs) are a type of implementation that uses solid materials, typically ceramics, as the ion-conducting electrolyte.[9–12] One of the most prominent compounds acting as a solid-state oxygen conductor in modern SOFC technologies is yttria-stabilized zirconia (YSZ).[11,13] Doping of ZrO_2 with other oxide materials such as Y_2O_3 is known to stabilize the cubic phase of zirconia. Due to the valence mismatch between Zr(IV) and Y(III), a vacancy in the anionic sublattice is created upon twofold substitution of Zr-atoms by Y. This is known to enable oxygen diffusion throughout the solid material.[14–16]

This property of YSZ, to function as a solid electrolyte, makes it an advanced material for SOFCs[11,13] and other applications, including oxygen sensors[17,18] and advanced catalysis procedures.[19,20] To achieve a sufficiently high diffusivity of the oxygen ions, comparably high operation temperatures in the range of 600 to 800 °C are required.[21,22] Therefore, finding alternative electrolyte materials with sufficient ion mobility below 700 °C is essential and a highly active field in contemporary research. One highly prominent alternative is gadolinia-doped ceria (GDC).[5,15,23] Similarly to YSZ, doping of CeO_2 with Gd_2O_3 introduces vacancies in the cubic crystal structure again promoting oxygen conduction. However, because of the increased ionic radii of Ce(IV) and Gd(III), the activation energy associated with the migration of oxygen atoms through the lattice is reduced compared to that of YSZ, thus resulting in enhanced diffusive properties at lower operating temperatures.

A promising route to study ion mobility in solid-state systems is the use of theoretical approaches such as molecular

Theoretical Chemistry Division Institute of General, Inorganic and Theoretical Chemistry Center for Chemistry and Biomedicine University of Innsbruck, Innrain 80–82, A-6020 Innsbruck, Austria. E-mail: T.Hofer@uibk.ac.at; Fax: +43-512-507-57199; Tel: +43-512-507-57111

† Electronic supplementary information (ESI) available. See DOI: https://doi.org/10.1039/d3cp05053j

dynamics (MD) simulations.[24] However, when considering the required system sizes and simulation periods to explicitly monitor ion diffusion in the long-time limit, the application of quantum chemical approaches, such as density functional theory (DFT), is typically not feasible, see Table S1 (ESI†). Therefore, a molecular mechanical (MM) method based on pre-parameterized potential functions describing interactions between all involved species provides the only viable alternative approach.[24] Although, MM-based MD simulations can easily reach the required simulation time to analyze the respective diffusion coefficient *D via* the associated mean-squared-displacement (MSD), an adequate parametrization of the model is a prerequisite to achieve accurate results. In a recent study, a parametrization strategy to obtain effective potential parameters for the description of ZrO_2, Y_2O_3, and YSZ has been outlined.[24] Although, several interaction potentials for these systems have already been described in the literature,[25–27] these potential models proved to be unsuitable for describing associated interface systems, *i.e.* simulation systems subject to 2D periodic boundary conditions.[24] The use of integer atomic charges derived from the formal oxidation number of ions in the material, *i.e.* $q_{Zr} = +4e$, $q_Y = +3e$, $q_O = -2e$ have been shown to cause nonphysical reorganization of both the surface as well as the bulk region, in the case of pure cubic ZrO_2.[24]

Similar to the case of YSZ and its constituents, there are only very few theoretical studies on GDC available in the literature. Gunn and co-workers[25] investigated the surface of gadolinia-doped ceria using a Monte Carlo simulation approach. As with most potential models developed for YSZ, the formal oxidation numbers of the respective ions were considered as integer charges, *i.e.* $q_{Ce} = +4e$, $q_{Gd} = +3e$ and $q_O = -2e$.

This work applies the previously described strategy used to obtain appropriate interaction potentials for ZrO_2, Y_2O_3, and YSZ to generate novel force field parameters for cubic CeO_2, Gd_2O_3, and GDC. This procedure facilitates effective partial charges rather than relying on integer atomic charges derived from formal oxidation numbers. In addition, the parametrization strategy was based on parameters obtained from a dissociative water model,[28,29] which should enable integration of the novel potential model. A recent study[30] showed that extending a dissociative water model by including solid-state parameters allows MM MD to describe surface phenomena of heterogeneous systems, such as SiO_2/H_2O. This framework provides a basis for simulating solid–liquid interfaces and describing surface protonation, which is a key step in the formation of a Helmholtz double layer and a fundamental step related to surface degradation.

To avoid the cost of using more expensive QM MD simulations (Table S1, ESI†) to analyze the vibrational properties of the target systems employed in the previous study of YSZ, a comparison of the harmonic vibrational modes with DFT-based frequency calculations has been carried out. The vibrational behavior of CeO_2 and Gd_2O_3 with the novel parameter set has been compared to DFT calculations.

Potential applications of this novel model in simulations of interfacial structures and 2D periodic QM/MM-type simulations are discussed in the conclusion.

2 Methods

2.1 Potential model

The parameters derived for CeO_2, Gd_2O_3, and GDC are based on a dissociative water model[28–31] previously developed for describing bulk water, oxonium (H_3O^+) and hydroxide (OH^-) ions along with their associated proton transfer reactions in solution. The main objective of the parametrization is to ensure compatibility between the novel derived solid-state potentials and the reactive water model.[28,29] The latter explicitly accounts for proton transfer reactions. Therefore, it is not possible to apply various atom types per element. All interactions, including those at liquid–solid interfaces, must be treated using the same potential model, regardless of the chemical species involved. Therefore, all O–O interactions should be treated using the same potential model, regardless of whether the oxygen atoms are part of the liquid or solid state. An MD simulation study of SiO_2/H_2O[30] demonstrates that the protonation of a solid oxygen atom through two successive proton transfer events could result in a water molecule that may dissociate into the liquid part of the simulation system. To ensure that the water molecule has the same properties as those of the bulk liquid, it is necessary to consider only a single type of oxygen.

The associated interaction potential consists of a Coulomb and a Buckingham term to describe the electrostatic and non-coulombic contributions between the atom pair *ij*

$$U_{ij}^{\mathrm{Coul}} = \frac{1}{4\pi\varepsilon_0}\frac{q_i q_j}{r_{ij}} = \frac{C_{ij}^{\mathrm{Coul}}}{r_{ij}} \quad (1)$$

$$U_{ij}^{\mathrm{Buck}} = A_{ij}\mathrm{e}^{-B_{ij}r_{ij}} + \frac{C_{ij}}{r_{ij}^6}, \quad (2)$$

with the respective pair distance given as r_{ij}. q_i, and q_j are the associated atomic partial charges, ε_0 corresponds to the permittivity of free space, and C_{ij}^{Coul} is the coulombic interaction parameter. The respective Buckingham interaction parameters are given as A_{ij}, B_{ij}, and C_{ij}.

A key prerequisite when applying dissociative molecular mechanical potentials is the employment of only a single atom type per element.[28,29,32] This is critical for the parametrization since oxygen atoms on the surface of a solid-state system can be transformed into H_2O through two consecutive protonation steps, thereby becoming part of the liquid state (or *vice versa*). As a result, the associated partial oxygen charge of $q_O = -0.898e$, applied to all oxygen atoms in the parametrization, is predetermined by the water potential.[28,29] The atomic charges of the cationic species are then determined to obtain neutral units of CeO_2 and Gd_2O_3. The respective values for q_{Ce} and q_{Gd} are thus given as $+1.796e$ and $+1.347e$, respectively. The same consideration also applies to non-coulombic contributions. Therefore, the use of the same Buckingham parameters as in the liquid is required for all O–O pairs irrespective of whether those are present in the solid or the liquid phase of a simulation system. For cation–cation (M–M) interactions, repulsive coulombic contributions are usually sufficient due to the contraction of the electron density, typically observed for

cations. As a result, the dispersive interaction (*i.e.* r^{-6}) is negligible, while the repulsive non-coulombic contributions are only significant for very small M–M distances (usually not observed in MD simulations, due to the small ionic radii). From this perspective, the only parameters required to formulate the interaction model are those associated with cation–anion interactions, *i.e.* $\{A, B, C\}_{ij}$ (i = Ce, Gd; J = O). However, a previous study focused on YSZ[24] has shown that due to the more complex crystal structure of yttria (space group $Ia\bar{3}$), it proved necessary to apply a non-coulombic Y–Y potential to achieve a structural description consistent with the experimental reference. Considering that Gd_2O_3 and Y_2O_3 are isotypic phases, it is reasonable to assume that a suitable non-coulombic M–M potential is necessary as well.

As discussed before, the formulation of the described interaction potential was particularly successful for the treatment of ZrO_2 and Y_2O_3, as well as modelling O diffusion in YSZ systems with various compositions.[24] It is expected that a similar successful result can be achieved in this study for the compounds under consideration.

2.2 Construction of the potential

In this work, the ion–oxygen interactions are described based on a coulombic (eqn (1)) plus Buckingham potential formulation (eqn (2)), leading to the following equation

$$U_{ij} = A_{ij}e^{-B_{ij}r_{ij}} + \frac{C_{ij}}{r_{ij}^6} + \frac{C_{ij}^{\mathrm{Coul}}}{r_{ij}}. \quad (3)$$

Aside from the aforementioned partial charges, the three Buckingham potential parameters must be specified for each type of interactions. As mentioned before, for the Ce–Ce interactions only the Coulomb term is required, as the non-Coulomb term can be expected to not contribute significantly to the total interaction potential.

The parameters – A_{ij}, B_{ij}, and C_{ij} – have been changed to adapt the system to the partial charges. However, when considering a specific cation–anion target distance r_{ij}^{eq} obtained from experimental reference data, the exponential prefactor A_{ij} can be determined from three parameters $\{r_{ij}^{\mathrm{eq}}, B_{ij}, C_{ij}\}$ *via*

$$\frac{\mathrm{d}U_{ij}}{\mathrm{d}r_{ij}} = -A_{ij}B_{ij}e^{-B_{ij}r_{ij}} - \frac{6C_{ij}}{r_{ij}^7} - \frac{C_{ij}^{\mathrm{Coul}}}{r_{ij}^2} = 0 \quad (4)$$

$$A_{ij} = -\frac{1}{B_{ij}}\left(\frac{6\cdot C_{ij}}{r_{ij}^7} + \frac{C_{ij}^{\mathrm{Coul}}}{r_{ij}^2}\right)e^{B_{ij}r_{ij}}\Bigg|_{r_{ij}=r_{ij}^{\mathrm{eq}}}. \quad (5)$$

The values for r_{ij}^{eq} were selected close to the experimental cation–anion equilibrium distance taken from the corresponding crystal structures, while B_{ij} and C_{ij} were systematically varied over a suitable search grid ranging from −20.0 to −4.0 Å^{-1} and −5000 to −200.0 Å^6 kcal mol^{-1}, respectively. Short-scale MD simulations were performed at 10 K for only 1 ps for each cation–anion interaction, defined by the three parameters $\{r_{ij}^{\mathrm{eq}}, B_{ij}, C_{ij}\}$, which is sufficient to estimate the density ρ. The various values for ρ obtained from the different simulations were then projected on the B_{ij} and C_{ij} plane, as depicted in Fig. 2. In addition, the thermal expansion was analyzed and compared to the reference for the selected parameters. Temperatures of 298.15, 698.15, 1098.15, and 1498.15 K were chosen.[33,34] Once agreement with the experimental densities had been reached, additional analysis was carried out to further refine the parameters.

2.3 Analysis

Both c-CeO_2 and c-Gd_2O_3 were analyzed in detail based on their densities and their ion–ion radial distribution functions (RDFs),[35] determined from the respective sampling period (*NPT* ensemble). In addition, vibrational power spectra have been determined *via* the Fourier transform of the velocity autocorrelation function (VACF)[35] $C(t)$ defined as follows

$$C(t) = \frac{\langle \mathbf{v}_0\mathbf{v}_t\rangle}{\langle \mathbf{v}_0\mathbf{v}_0\rangle}, \quad (6)$$

where $\mathbf{v}_t$ and $\mathbf{v}_0$ are the velocity vectors of all atoms in the system at time t and at the time origin t = 0, respectively. The correlation window consisted of a time interval of 0.5 ps. The Fourier transform was then performed by applying an exponential window function with a factor of 4 ps^{-1}.

To analyze the oxygen diffusion in the GDC system, the Einstein relation[35] was used, which is expressed as

$$D = \frac{1}{2d}\lim_{t\to\infty}\frac{\left\langle \|\mathbf{r}_t - \mathbf{r}_0\|^2\right\rangle}{t}, \quad (7)$$

with d being the dimension of the system's diffusion vector (here d = 3); $\mathbf{r}_t$ and $\mathbf{r}_0$ correspond to the position vectors of an oxygen atom at time t and at the time origin t = 0, respectively. A correlation length of 100 ps proved sufficient to study O-diffusion in GDC. In the analysis, only the last 10 ps were considered for the linear regression to estimate the diffusion coefficient. Generally, the diffusion coefficient D is well-described by the Arrhenius equation

$$D = D_0\cdot e^{-E_A/RT}, \quad (8)$$

where D_0 is the pre-exponential factor, E_A the activation energy, T the temperature and R the molar gas constant. A linearized version of the equation

$$\ln(D) = \ln(D_0) - \frac{E_A}{R}\cdot\frac{1}{T} \quad (9)$$

is used to calculate E_A from the slope of the Arrhenius representation.

The calculation of the vibrational modes requires the construction of the Hessian matrix **H**. Individual single-point calculations were performed with each atom of the minimized structure being displaced in each dimension for a certain Δr, which for this specific work was set to ±0.01 Å. **H** was then constructed *via* numerical differentiation of the individual forces $\mathbf{f}_{i\mu}$

$$\mathbf{h}_{i\mu} = \frac{\partial \mathbf{f}_{i\mu}}{\partial r_{i\mu}} = \frac{\mathbf{f}_{i\mu}(r_{i\mu}+\Delta r) - \mathbf{f}_{i\mu}(r_{i\mu}-\Delta r)}{2\Delta r} \quad \mu = \{x, y, z\} \quad (10)$$

with $r_{i\mu}$ being a vector component of the atom i. The resulting gradient $\mathbf{h}_{i\mu}$ corresponds to a single column of $\mathbf{H}$. After evaluation of all $\mathbf{h}_{i\mu}$ contributions, $\mathbf{H}$ has been symmetrized according to

$$\mathbf{H}' = \mathbf{H}^{\mathrm{T}}\mathbf{H} \tag{11}$$

$$\mathbf{u} = \mathbf{U}^{\mathrm{T}}\mathbf{H}'\mathbf{U} \tag{12}$$

$$\mathbf{H}_{\mathrm{CART}} = \mathbf{H}^{1/2} = \mathbf{U}^{\mathrm{T}}\sqrt{\mathbf{u}}\mathbf{U} \tag{13}$$

to limit numerical instabilities by ensuring real eigenvalues of the $\mathbf{H}$.[36] The eigenvectors and eigenvalues of $\mathbf{H}'$ are denoted as $\mathbf{U}$ and $\mathbf{u}$, respectively. Once the symmetrized Hessian $\mathbf{H}_{\mathrm{CART}}$ was obtained, the vibrational analysis was performed according to the procedure described by Ochterski.[36] The calculations were performed using the VibrationalAnalysis.jl package (version 0.1.5).[37]

2.4 MD simulation protocol

The MD simulations were performed using the velocity Verlet algorithm[38] with a time step of 2 fs. To simulate the system in the *NPT* ensemble, pressure and temperature control was performed using the Berendsen weak coupling manostat and thermostat algorithms,[39] with relaxation times set to $\tau_{\mathrm{p}} = 1.0$ ps and $\tau_{\mathrm{T}} = 0.1$ ps, respectively. The Wolf summation technique[40] was used to account for long-range coulombic contributions, employing a cutoff distance of 10 Å and a damping factor $\kappa = 0.22$ Å^{-1}.

For the potential construction, the systems were equilibrated at 10 K and 1.013 bar for 0.5 ps, followed by a 0.5 ps sampling period. The analysis of the RDF and VACF required 50 ps equilibration and a sampling period of 100 ps. The diffusion coefficient calculations used different GDC systems, which were equilibrated for 50 ps, with a subsequent sampling period of 5 ns.

2.5 System setup

The experimental crystal structures of the cubic unit cells were obtained from the Crystallography Open Database (COD).[41–47] CeO_2 has a unit cell length of 5.411 Å (space group number 225, COD entry 9009008[48]). In the case of Gd_2O_3, the unit cell length is 10.79 Å (space group number 199, COD entry 1010338[49]), see Fig. 1. The cubic supercells of CeO_2 and Gd_2O_3 contained $5 \times 5 \times 5$ and $3 \times 3 \times 3$ unit cells with a total of 1500 and 2160 atoms, respectively. To counteract possible simulation artifacts arising from an ideal placement of atoms in the periodic crystal, a random modification of the atomic positions in the initial structure was carried out by up to $\pm 10^{-2}$ Å along every principal axis.

The GDC systems were created by using the cubic CeO_2 supercell, in which Ce was randomly substituted by Gd atoms. To maintain charge neutrality, one randomly selected oxide anion was removed per two cationic substitutions, resulting in vacancies in the lattice to promote oxygen conduction. Table 1 specifies the various GDC systems investigated in this study.

For the harmonic vibrational analysis, supercells with dimensions of $4 \times 4 \times 4$ (768 atoms) and $2 \times 2 \times 2$ (640 atoms) unit cells were used for CeO_2 and Gd_2O_3, respectively.

2.6 Reference DFT Calculations

DFT calculations were conducted using the CRYSTAL23 program[50] employing the HSEsol[51,52] functional in combination with basis sets featuring ECPs developed by El-Kelany[53] and Desmarais[54] for Ce and Gd. A double zeta valence basis set reported by Vilela-Oliveira[55] was assigned to the oxygen atoms in both solids. The structures of the system have been optimized prior to the frequency calculation.

3 Results and discussion

3.1 Potential construction

For CeO_2, the reference point for the theoretical equilibrium distance was taken from the respective crystal structure (COD entry 9009008[48]) as $r^{\mathrm{eq}}_{\mathrm{Ce-O}} = 2.34$ Å. The results indicate a slightly lower equilibrium distance at $r_{\mathrm{Ce-O}} = 2.24$ Å, consistent with the previously recorded values in the study of ZrO_2.[24] Sameshima *et al.*[34] reported the density of CeO_2 at 298 K and 1.013 bar to be

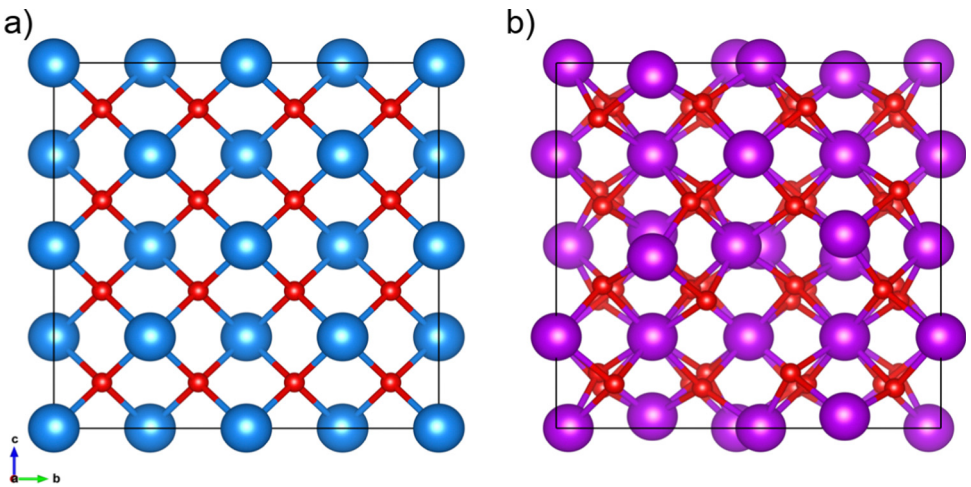

Fig. 1 (a) $2 \times 2 \times 2$ supercell of cubic CeO_2 (COD entry 9009008[48]) with a unit cell length of $2a = 10.822$ Å and (b) unit cell of Gd_2O_3 (COD entry 1010338[49]) with a unit cell length of 10.79 Å. Red spheres represent the oxygen atoms, while the blue and purple spheres represent Ce and Gd atoms, respectively.

Table 1 Number of individual units of CeO_2 and Gd_2O_3 for various mol% of GDC

	$x_{Gd_2O_3}$/%	N_{CeO_2}	$N_{Gd_2O_3}$	N_{atoms}
GDC04	3.95	462	19	1481
GDC5.3	5.30	450	25	1475
GDC06	5.93	444	28	1472
GDC07	7.07	434	33	1467
GDC08	7.99	426	37	1463
GDC09	8.93	418	41	1459
GDC10	9.89	410	45	1455
GDC11	11.11	400	50	1450
GDC12	11.86	394	53	1447
GDC13	13.12	384	58	1442
GDC14	13.90	378	61	1439
GDC15	14.94	370	65	1435

7.218 g cm^{-3}, corresponding to a lattice parameter of the cubic unit cell a = 5.410 Å. The calculated density at standard conditions obtained in this work is 7.216 g cm^{-3} (a = 5.410 Å) and agrees perfectly with the experimental value. When using the potential reported by Gunn *et al.*,[25] the calculated equilibrium density at these simulation settings amounts to 7.316 g cm^{-3} (a = 5.386 Å).

The most accurate results for Gd_2O_3 were achieved through a parameter scan based on a Gd–O radius of r^{eq}_{Gd-O} = 2.21 Å. However, the RDF analysis revealed that the peaks in the Gd–Gd distribution were not in ideal agreement as previously also observed in the case of Y_2O_3.[24] Consequently, a non-coulombic Gd–Gd potential had to be constructed using the equilibrium radius of r^{eq}_{Gd-Gd} = 3.85 Å, which is located between the first two ideal crystal pair distributions. After the addition of the Gd–Gd non-coulombic pair potential, the density of Gd_2O_3 was determined to be 7.677 g cm^{-3} with a corresponding value for a = 10.79 Å at standard conditions, which is in good agreement with Krishnan *et al.*,[33] who reported the density of cubic Gd_2O_3 to be 7.664 g cm^{-3} (a = 10.80 Å). Conversely, the potential reported by Gunn *et al.* estimated the density to be 8.406 g cm^{-3} (a = 10.46 Å), which is significantly higher than the experimental value by approx. 10%.

For GDC, the pair potential parameters were obtained by combining the potential parameters for Gd_2O_3 and CeO_2, as listed in Table 2. The parameters for the Ce–Gd interaction were added, comprising solely of a repulsive Coulomb term.

Table 2 Buckingham potential parameters A, B and C for each of the possible ion–ion pairs in GDC derived in this work

	A_{ij}/kcal mol^{-1}	B_{ij}/$Å^{-1}$	C_{ij}/$Å^6$ kcal mol^{-1}
Ce–Ce	—	—	—
Ce–Gd	—	—	—
Gd–Gd	7.6481×10^{12}	8.2029	−3491.6
Ce–O	7.2958×10^{16}	16.4572	−500.0
Gd–O	7.5282×10^{9}	8.7830	−4500.0
O–O	2.7970×10^{5}	4.0199	−835.0

3.2 Radial distribution

The RDFs of CeO_2 and Gd_2O_3 were calculated to characterize the respective structural properties. To evaluate the thermal stability of the newly parametrized interaction model, RDFs were calculated for simulations conducted at 298.15, 698.15, 1098.15, and 1498.15 K. The RDFs of CeO_2 and Gd_2O_3 are shown in Fig. 3 and 5, respectively. Moreover, a comparison of the RDFs at 298 K with the potential reported by Gunn *et al.*[25] is presented in Fig. S1 and S2 (ESI†).

Fig. 3 displays the RDFs of all ion pairs of CeO_2 over a wide temperature range. The pair distributions are in perfect agreement with the experimental values estimated based on the crystal structure reported by Wyckoff.[48] Furthermore, the distribution at larger distances is also accurately represented, showing that the crystal structure is well portrayed in the short-range as well as the long-range order. At higher temperatures, it is apparent that the distributions are slightly shifted towards larger distances, which is a result of the thermal expansion of the crystal. Fig. S2 (ESI†) compares the RDFs from this work to the RDFs of the potential reported by Gunn *et al.* The reference distribution appears to be broader, indicating higher atom mobility. Nevertheless, the maxima of the distributions appear at the same distance values, suggesting that the reference potential also accurately describes the crystal structure, although with a slight but noticeable shift towards shorter interatomic distances.

For Gd_2O_3, a non-coulombic potential was added to account for the initial mismatch in the RDF of the Gd–Gd pair distribution, as shown in Fig. 4. The introduction of the non-coulombic cation–cation potential greatly improved the distribution, as can be seen in the RDFs shown in Fig. 5. The pair distributions are in perfect agreement with the distribution determined from the experimental crystal structure. The off-axis displacement of the oxygen atoms (Fig. 1(b)) results in a higher degree of disorder in Gd_2O_3. For this reason, the pair distributions including oxygen atoms show a higher number of peaks, as seen in Fig. 5(a) and (b). This disorder cannot be observed in the RDFs because a thermally averaged ensemble is analyzed. Nevertheless, it can be concluded that the crystal structure is accurately represented. When compared to the potential of Gunn *et al.* shown in Fig. S2 (ESI†), which overall displays a significant shift to lower distances, the newly parametrized potential provides an improved description of cubic Gd_2O_3. The large deviation was already apparent when comparing the obtained densities to the experimental value as discussed before.

3.3 Surface stability

One of the main motivations for the development of the novel potential was the improvement of the surface stability enabling simulation studies of surface processes, *e.g.* surface protonation using a dissociative water model. This is particularly important when simulating solid/gas interfaces or materials in contact with liquid water as surface protonation facilitates surface degradation. Solid–liquid interfaces are typically simulated using a 2D treatment for the solid, necessitating a potential that is capable of describing the surface without any nonphysical surface reconstruction, as also reported for ZrO_2 and Y_2O_3.[24] Surface reconstruction usually results in a rearrangement of surface atoms, however, it should have no impact on

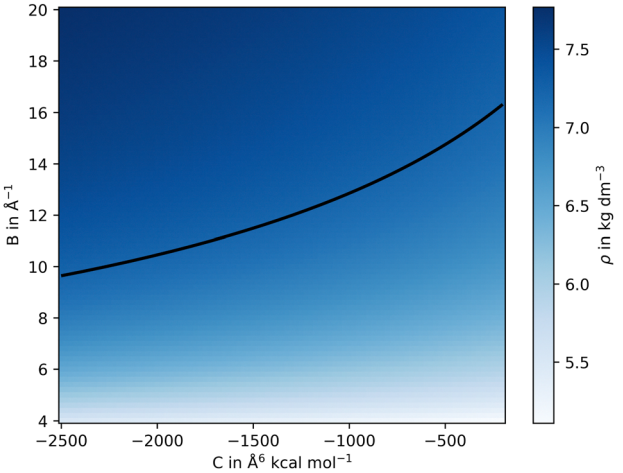

Fig. 2 2D representation of the resulting density obtained from a scan performed over parameters B and C of the Buckingham potential at the example of CeO_2. The iso-density line (shown in black) is set to the experimental reference value of 7.218 g cm^{-3}.[34] Three selected points of the iso-density were taken to further refine the non-coulombic potential, here C = −200, −1125 and −2500 Å^6 kcal mol^{-1}.

the bulk properties of the investigated solid. This leads to a non-ideal description of the crystal structure. Thus, partial charge models, which are compatible with water models, are a prerequisite to accurately represent material surfaces. In contrast, integer-charge models, typically used to describe the bulk of the material, are in general not compatible with other potential models based on effective partial charges.

The surface stability was tested through the construction of various interfacial systems, followed by simulating these structures at different temperatures using a 2D periodic pressure control. These surfaces comprised slabs of CeO_2 and Gd_2O_3 with (001), (101) and (111) orientations. The simulations were conducted over a temperature range of 10 to 2000 K.

The (001) surface is known to be polar and, therefore, expected to be less stable on the surface, however, it was found to remain stable at lower temperatures. Fig. S3 (ESI†) displays the surface stability of (001) when compared to the full charge potential of Gunn *et al.*[25] The latter case reveals deviations from the ideal crystal geometry observed near the surface propagating into the bulk, which is a prime example of nonphysical surface reconstruction. For the (101) plane of CeO_2, it was also discovered that the surface is highly stable. The structural motif agrees with the bulk structure, although featuring minor deviations in the surface region. With the potential of Gunn *et al.*, the bulk shows a significant deviation from the bulk crystal structure. In the case of the (111) surface, the 2D periodic crystal was found to be stable at all temperatures for both potentials.

In contrast, the (001) surface of Gd_2O_3 was found to be less stable than that of CeO_2, seen in Fig. S4 (ESI†). Compared to Gunn *et al.*,[25] the (101) and (111) surface structures were found to perform similarly. However, when using a (001) surface, the partial-charge potential model utilized in this work performs much better without major surface reconstruction. For the

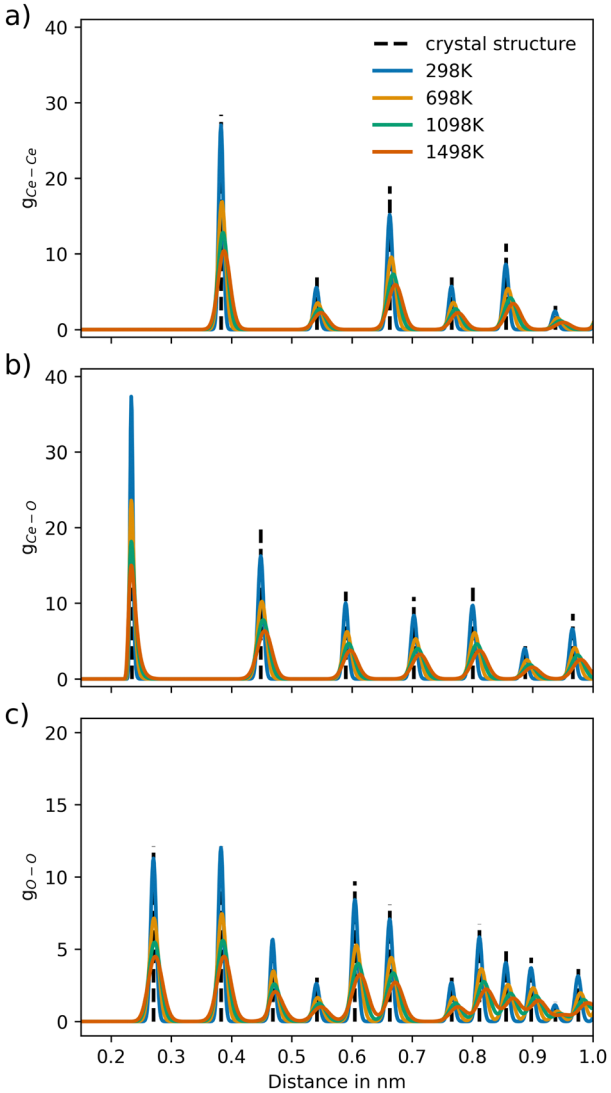

Fig. 3 Ion–ion pair distribution for CeO_2 over different temperature settings for the pairs (a) Ce–Ce, (b) Ce–O and (c) O–O, respectively. The dashed vertical lines represent the pair distances of the associated crystal structure (COD entry 9009008[48]).

potential of Gunn *et al.*, the surface reconstruction is visible, which can be attributed to the use of the formal atomic charges employed in this interaction model.

Thus, the novel potential presented in this work is capable of describing the surface of CeO_2 and Gd_2O_3 without any major surface reconstruction, which was one of the main goals of the parametrization. This represents a significant improvement over the potential of Gunn *et al.*

3.4 Oxygen diffusion in GDC

The oxygen diffusion in GDC was analyzed to determine the diffusion coefficient and the associated activation energy. Equilibration included a 50 ps heating and pressurization period. Afterwards, sampling was conducted for 5 ns by simulating the GDC systems at 800, 1000, 1200, 1400, 1600, and 1800 K following equilibration to ensure much longer

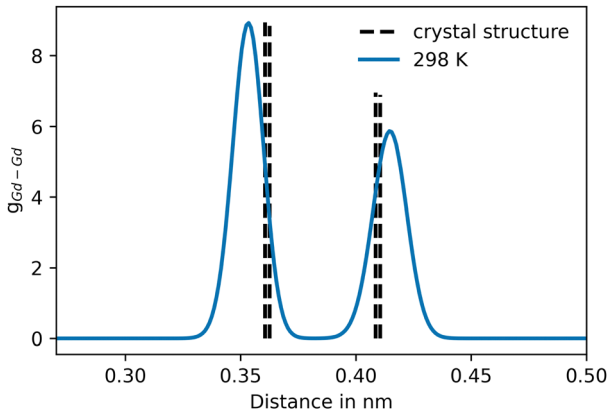

Fig. 4 Pair distribution of the initial Gd–Gd distribution, prior to the addition of the non-coulombic cation–cation potential contribution. The dashed vertical lines represent the pair distances of Gd–Gd in the associated crystal structure (COD entry 1010338[49]).

simulation periods compared to the correlation length used in the determination of the diffusion coefficient D.

Fig. 6 shows the oxygen diffusion in GDC at different temperatures and mole percentages of Gd_2O_3, in comparison to the potential of Gunn *et al.*[25] Significant variations in the diffusion coefficient can be observed between the different GDC systems at lower temperatures due to a lower number of individual diffusion events. Fewer sampled oxygen transitions lead to larger variations in the calculated diffusion coefficients, which is especially visible at 800 K. At higher temperatures, the variance in the diffusion coefficient is reduced, as the atoms are more mobile and oxygen diffusion is more likely to occur. Compared to Gunn *et al.*, the diffusion coefficients are significantly higher at all temperatures and mole percentages of Gd_2O_3, by at least one order of magnitude.

Fig. 7(a) depicts the linearized Arrhenius representation (eqn (9)) of O diffusion in GDC at 5.3 mol% of Gd_2O_3 (GDC5.3). The diffusion coefficients accurately follow the experimental trend reported by Manning *et al.*[56] Conversely, the oxygen diffusion using the potential of Gunn *et al.* is lower than the experimental values by up to one order of magnitude. In addition, further experimental data from Ruiz-Trejo *et al.*[57] was included, which was reported for a GDC system including 18.3 mol% Gd_2O_3. The experimental data from Ruiz-Trejo *et al.* shows a significantly larger slope, implying that the activation energy increases with higher concentrations of Gd_2O_3.

The activation energy at different Gd_2O_3 concentrations is shown in Fig. 7(b). At 5.3 mol% the E_A using the potential of Gunn *et al.* with 0.706 eV does more closely match the 0.724 eV reported by Manning *et al.* However, the E_A remains at constant values for higher concentrations of Gd_2O_3. The activation energy using the potential of this work resulted in a value at 5.3 mol% of 0.688 eV, which deviates by approximately 0.03 eV from the experimental value. The higher value can be explained to be most likely due to statistical deviation. The overall tendency is towards higher E_A with higher mol%. The E_A of 1.15 eV at 18.3 mol% reported by Ruiz-Trejo *et al.* is in line with our findings, indicating that at higher concentrations the

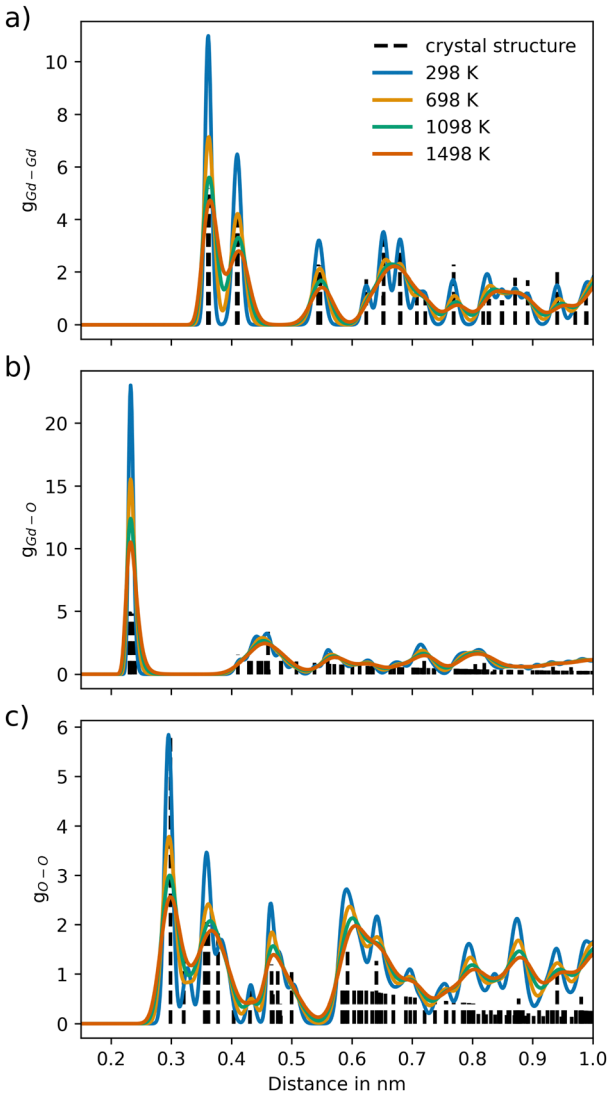

Fig. 5 Ion–ion pair distribution for Gd_2O_3 over different temperature settings for the pairs (a) Gd–Gd, (b) Gd–O and (c) O–O, respectively. The dashed vertical lines represent the pair distances of the associated crystal structure (COD entry 1010338[49]).

activation energy increases. This is also consistent with the results observed previously for YSZ.[24]

3.5 Vibrational power spectrum

To analyze the VACF, individual simulations of 20 ps and a sampling frequency of 1 MD step were executed, which were started from an already pre-equilibrated configuration. As shown in the previous study of YSZ,[24] due to averaging over many atoms and the short-time nature of the atomic vibrations, short trajectories proved to be sufficient to obtain reliable estimations of the respective vibrational power spectra.

Additionally, as a reference for the vibrational properties of c-CeO_2 and c-Gd_2O_3, calculations were performed using the potential of Gunn *et al.*[25] The power spectrum of CeO_2 (Fig. 8(a)) reveals a more narrow spectral distribution that is overall shifted to higher wave numbers. Nevertheless, the

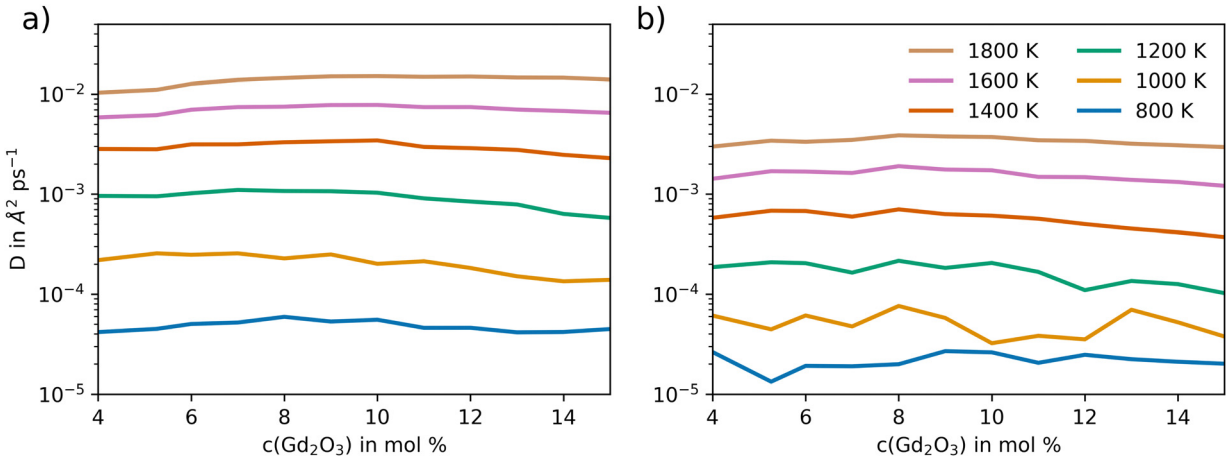

Fig. 6 Self-diffusion coefficient of oxygen atoms in GDC as a function of Gd_2O_3 concentration and temperature obtained *via* extended MD simulations using (a) the newly developed potential model and (b) the potential reported by Gunn *et al.*[25]

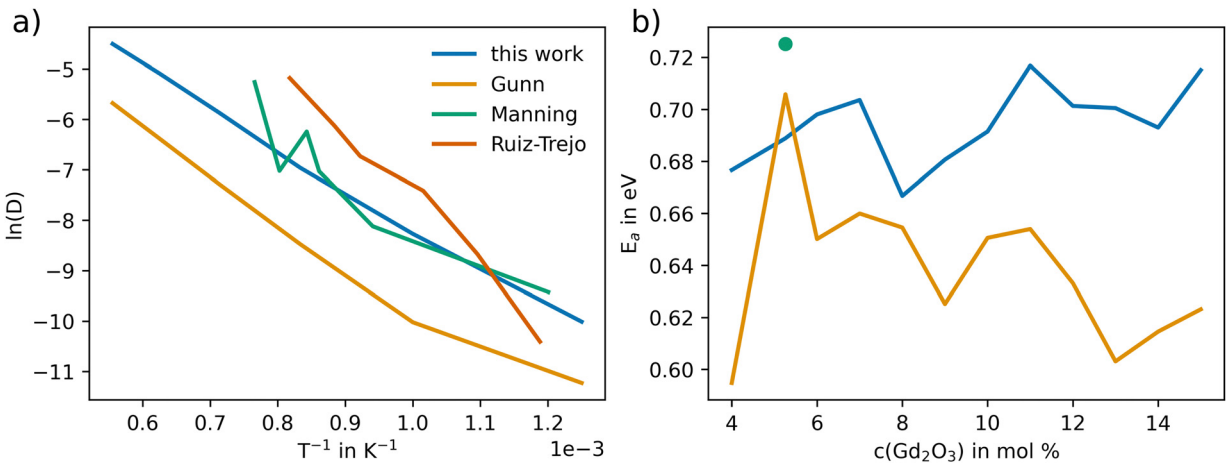

Fig. 7 Arrhenius representation of the oxygen diffusion coefficient (D in Å^{-2} ps^{-1}) in GDC (5.3% Gd_2O_3) obtained *via* MD simulations employing the potential derived in this work in comparison to results obtained *via* the potential model of Gunn *et al.*[25] and experimental data from Manning *et al.*[56] In addition, the results of Ruiz-Trejo *et al.*[57] at 18.36 mol% are shown. (b) Activation energy E_A obtained for different mol% of Gd_2O_3 in GDC including the results reported by Manning *et al.*[56] The E_A value resulting from the data of Ruiz-Trejo *et al.*[57] of 1.15 eV is not shown in the figure.

potential developed in this work is capable of describing the crystal in a similar way, as the bands appear in nearly the same wave number range. For Gd_2O_3 the vibrational power spectrum (Fig. 8(b)) shows substantial similarity to the reference. However, as in the case of CeO_2, higher wave numbers compared to the potential of Gunn *et al.* can be observed. This points towards different curvatures in the two potential formulations.

The vibrational power spectra for both CeO_2 and Gd_2O_3 are shifted to higher wave numbers in both cases, indicating slightly increased effective force constant resulting in more tightly bond ion-pairs as already seen in the RDFs that were compared to the reference potential, see Fig. S1 and S2 (ESI†).

3.6 Harmonic frequency spectrum

There are limitations in comparing the vibrational power spectra obtained from different force field potentials. The high cost involved in producing a vibrational power spectrum and the inability to distinguish between infrared- and Raman-active modes through a QM MD calculation, led to the eventual addition of the vibrational analysis. A comparison between the cost of the harmonic frequency calculation and the vibrational power spectrum is shown in Table S1 (ESI†). The harmonic infrared spectrum is compared to the spectrum resulting from the potential of Gunn *et al.*[25] As a reference to the results obtained by both potentials, a DFT frequency calculation was added, as shown in Fig. 9.

To conduct the harmonic vibrational analysis, the systems were minimized using the respective parameter sets. To reduce the computational demand, the supercell dimensions were kept to a minimal size, while still maintaining consistency with the Coulomb cutoff distance. As a result, the supercell sizes were set to $4 \times 4 \times 4$ and $2 \times 2 \times 2$ unit cells in the case of CeO_2 and Gd_2O_3, respectively.

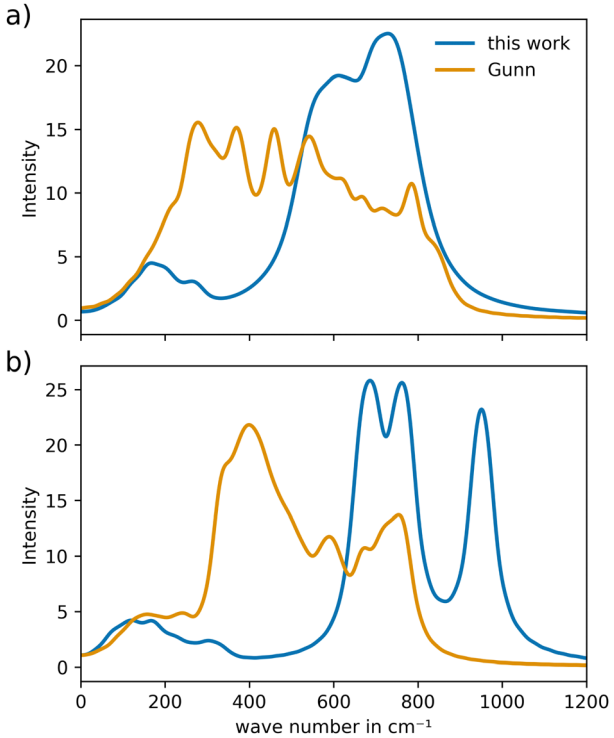

Fig. 8 Comparison of the vibrational power spectra of (a) CeO_2 and (b) Gd_2O_3 obtained from the novel potential and the potential reported by Gunn *et al.*[25]

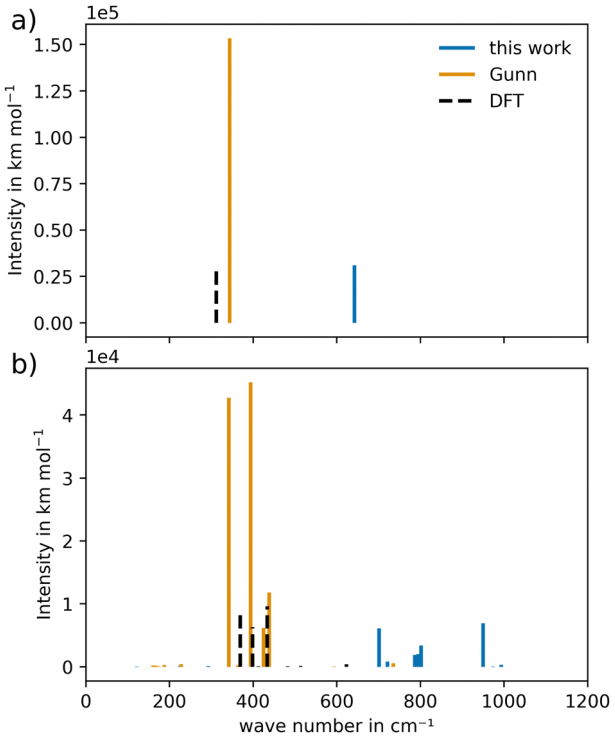

Fig. 9 Harmonic infrared spectra of (a) CeO_2 and (b) Gd_2O_3 of the newly constructed potential compared to Gunn *et al.*[25] and DFT calculations at HSEsol level.

For CeO_2, the IR active frequency modes display good agreement with the DFT calculations, as shown in Fig. 9(a). The band shows a slight blue shift, suggesting a higher effective curvature in the potential. In contrast, the potential of Gunn *et al.* displays modes that closely match the wave number of the DFT calculation, indicating that the lower curvature is a more appropriate description of the system's vibrational properties. On the other hand, peak intensities differ significantly due to the different charge models. The potential of Gunn *et al.* uses integer charges, while the novel potential is based on partial atomic charges. This in turn leads to a lower intensity in the latter case that is more in line with the results determined by the DFT calculation. In the case of CeO_2, the vibrational behavior suggests that additional adjustments to the potential parameters would be necessary to obtain a more accurate description of the wave numbers. However, from the perspective of the intensities, the novel potential model seems to be more suitable for the description of the vibrational properties.

In the case of Gd_2O_3, a similar result was obtained, shown in Fig. 9(b). The wave numbers observed for the novel potential are again blue-shifted, indicating a higher curvature in the potential between the ion pairs. The wave numbers of the potential of Gunn *et al.* are in line with the results obtained from the DFT frequency calculation. The increased number of visible frequency modes could be attributed to the disordered position of the O atoms in the crystal structure, illustrated in Fig. 1(b). This renders the crystal structure less ideal compared to that of CeO_2. Additionally, the intensities, when compared to the DFT calculations, are similar to the result obtained for CeO_2.

Fig. S5 (ESI†) shows the comparison of the spectra obtained from the harmonic frequency calculation with those determined *via* the MD simulation, *i.e.* vibrational power spectrum, for CeO_2 and Gd_2O_3. The results are in good agreement, showing that the harmonic frequency calculation is a good replacement for the vibrational power spectrum since the latter is much more computationally demanding.

3.7 Comparison of the M–O potential

In Fig. S6a and b (ESI†) the M–O contribution of both the newly developed potential and those published by Gunn *et al.*[25] are compared. At first sight, several notable differences are visible, foremost the strongly differing magnitude of the interaction. The latter is a direct result of the different partial charges employed in the model, which in turn result in differences in the coulombic contributions. Although these differences are compensated by the corresponding M–M and O–O interactions, it can be seen that they have a notable impact on the curvature of the potential near the minimum distances, which directly influences the vibrational wave numbers. However, when comparing the respective equilibrium distances in the M–O interactions, it is evident that the minima observed in the potential by Gunn *et al.* does not coincide with the ion–oxygen pair distance in the crystal structure. In fact, the minimum distances deviate from the M–O equilibrium distance by approx.

0.60 and 0.55 Å in case of CeO_2 and Gd_2O_3, respectively (see also comparison in Fig. S6c and d, ESI†). This implies that in the simulation the correct M–O distances are only formed due to an error compensation between the attractive M–O interaction and the repulsive M–M and O–O contributions.

In contrast, the equilibrium positions in the newly developed model are perfectly aligned with the expected M–O distances. However, this property comes at the price of a much steeper repulsive branch in the M–O contributions, which ultimately influences the vibrational wave numbers in a negative way. While it would be certainly possible to adjust the curvature of the potential to improve this particular aspect, it can be expected that other properties such as the lattice constant/density and O-diffusivity would be negatively impacted. In order to properly adjust the vibrational properties without introducing any additional shortcomings, a more complex description of the interactions beyond the capabilities of a pairwise additive Coulomb plus Buckingham potential would be required. While this not only requires a more complicated parametrization procedure, the use of uncommon functional forms of the potential greatly reduces the benefit of the newly derived interaction model, as alternative potentials are commonly not available in the majority of the available simulation packages.

4 Conclusion and outlook

In this work, a newly parametrized set of interaction potentials aimed at the description of CeO_2, Gd_2O_3 and GDC has been derived based on the strategy already applied successfully in the case of ZrO_2, Y_2O_3 and YSZ.[24] Again, the use of atomic partial charges in the potentials significantly enhances the description of the crystal structure, as demonstrated by the RDFs as well as the density values. The surface stability was also greatly improved over existing potential models for all surfaces tested. Additionally, the use of a non-coulombic Gd–Gd pair potential greatly enhanced the description of Gd_2O_3, which was not accounted for in the potential of Gunn *et al.*[25]

Application of this potential significantly improved the oxygen diffusivity by at least one order of magnitude compared to an early potential model reported by Gunn *et al.* Furthermore, the tendency of the activation energy with increasing concentration is in good agreement with the experimental data provided by Manning *et al.*[56] and Ruiz-Trejo *et al.*[57]

However, a detailed analysis of the vibrational properties employing both harmonic frequency calculations as well as VACFs analyzed over the MD trajectory revealed, that the wave numbers obtained using the description of Gunn *et al.* are in better agreement with results obtained *via* DFT calculations at HSEsol level of theory, while the observed intensities of the vibrations are more in line with the results obtained from the novel potential formulation.

Based on a detailed comparison of the associated M–O potentials it was shown that the newly developed potential is capable of describing the crystal structure more accurately, as the equilibrium distances are in perfect agreement with the crystal structure. In contrast, the potential by Gunn *et al.* does not accurately describe the crystal structure, as the equilibrium distances deviate from those observed in the crystal structure. While this shortcoming has an overall positive influence on the vibrational wave numbers, it implies that the correct M–O distances are only formed due to an error compensation between the attractive M–O interaction and the repulsive M–M and O–O contributions. This, on the other hand, explains the deviations in the ion diffusion as well as the too large density observed in the case of Gd_2O_3.

The newly developed potential presented in the work was shown to successfully describe the crystal structure of CeO_2 and Gd_2O_3 at ambient conditions and elevated temperatures. The benefit of using partial charges is that the model can be used in conjunction with existing partial charge models such as a reactive water model developed earlier by Wiedemair[28,29] as well as force fields aimed at the description of organic and biomolecular systems.[58,59] This would enable simulations of surface processes such as the formation of a Helmholtz double layer and associated reactive corrosion process as well as the adsorption of organic molecules at GDC interfaces in the presence of liquid water. Furthermore, it enables in-depth analysis of surface reactions, such as water dissociation and surface hydroxyl group formation, without requiring a complex and computationally expensive *ab initio* approach. However, these reactive potentials would facilitate a QM/MM approach, which would allow for a more detailed description of the surface processes. In addition, the effect of surface protonation on the oxygen diffusivity and overall performance of different GDC systems in solid oxide fuel cells and electrolyzers can be thoroughly examined. This is because diffusion phenomena can only be observed using larger time scales and system sizes, which are made possible by the newly developed potential.

Conflicts of interest

There are no conflicts to declare.

Acknowledgements

The computational results presented were achieved (in part) using the HPC infrastructure of the University of Innsbruck.

References

1 M. K. Singla, P. Nijhawan and A. S. Oberoi, Hydrogen fuel and fuel cell technology for cleaner future: a review, *Environ. Sci. Pollut. Res.*, 2021, **28**, 15607–15626.
2 P. R. Shukla, J. Skea, R. Slade, A. Al Khourdajie, R. van Diemen, D. McCollum, M. Pathak, S. Some, P. Vyas, R. Fradera, M. Belkacemi, A. Hasija, G. Lisboa, S. Luz and J. Malley, *Climate Change 2022 – Mitigation of Climate Change: Working Group III Contribution to the Sixth Assessment Report of the Intergovernmental Panel on Climate Change*, Cambridge University Press, 2023, pp.51–148.

3 D. A. Cullen, K. C. Neyerlin, R. K. Ahluwalia, R. Mukundan, K. L. More, R. L. Borup, A. Z. Weber, D. J. Myers and A. Kusoglu, New roads and challenges for fuel cells in heavy-duty transportation, *Nat. Energy*, 2021, **6**, 462–474.
4 T. Kadyk, R. Schenkendorf, S. Hawner, B. Yildiz and U. Römer, Design of Fuel Cell Systems for Aviation: Representative Mission Profiles and Sensitivity Analyses, *Front. Energy Res.*, 2019, **7**, 35.
5 N. Brandon, S. Skinner and B. Steele, Recent Advances in Materials for Fuel Cells, *Annu. Rev. Mater. Res.*, 2003, **33**, 183–213.
6 D. Cheddie and N. Munroe, Review and comparison of approaches to proton exchange membrane fuel cell modeling, *J. Power Sources*, 2005, **147**, 72–84.
7 N. Mohammad, A. B. Mohamad, A. A. H. Kadhum and K. S. Loh, A review on synthesis and characterization of solid acid materials for fuel cell applications, *J. Power Sources*, 2016, **322**, 77–92.
8 T. Ferriday and P. H. Middleton, Alkaline fuel cell technology - A review, *Int. J. Hydrogen Energy*, 2021, **46**, 18489–18510.
9 S. J. Skinner and J. A. Kilner, Oxygen ion conductors, *Mater. Today*, 2003, **6**, 30–37.
10 J. W. Fergus, Electrolytes for solid oxide fuel cells, *J. Power Sources*, 2006, **162**, 30–40.
11 S. Y. Gómez and D. Hotza, Current developments in reversible solid oxide fuel cells, *Renewable Sustainable Energy Rev.*, 2016, **61**, 155–174.
12 F. S. da Silva and T. M. de Souza, Novel materials for solid oxide fuel cell technologies: A literature review, *Int. J. Hydrogen Energy*, 2017, **42**, 26020–26036.
13 B. S. Prakash, S. S. Kumar and S. Aruna, Properties and development of Ni/YSZ as an anode material in solid oxide fuel cell: A review, *Renewable Sustainable Energy Rev.*, 2014, **36**, 149–179.
14 H. L. Tuller and A. S. Nowick, Doped Ceria as a Solid Oxide Electrolyte, *J. Electrochem. Soc.*, 1975, **122**, 255–259.
15 B. Steele, Appraisal of $Ce_{1-y}Gd_yO_{2-y/2}$ electrolytes for IT-SOFC operation at 500 °C, *Solid State Ionics*, 2000, **129**, 95–110.
16 J. Koettgen, S. Grieshammer, P. Hein, B. O. H. Grope, M. Nakayama and M. Martin, Understanding the ionic conductivity maximum in doped ceria: trapping and blocking, *Phys. Chem. Chem. Phys.*, 2018, **20**, 14291–14321.
17 T. Liu, X. Zhang, L. Yuan and J. Yu, A review of high-temperature electrochemical sensors based on stabilized zirconia, *Solid State Ionics*, 2015, **283**, 91–102.
18 A. Iio, H. Ikeda, S. A. Anggraini and N. Miura, Sensing characteristics of YSZ-based oxygen sensors attached with $Ba_xSr_{1-x}FeO_3$ sensing-electrode, *Solid State Ionics*, 2016, **285**, 234–238.
19 P. Wózniak, M. A. Małecka, P. Kraszkiewicz, W. Miśta, O. Bezkrovnyi, L. Chinchilla and S. Trasobares, Confinement of nano-gold in 3D hierarchically structured gadolinium-doped ceria mesocrystal: synergistic effect of chemical composition and structural hierarchy in CO and propane oxidation, *Catal. Sci. Technol.*, 2022, **12**, 7082–7113.
20 A. Bhalkikar, T.-S. Wu, T. J. Fisher, A. Sarella, D. Zhang, Y. Gao, Y.-L. Soo and C. L. Cheung, Tunable catalytic activity of gadolinium-doped ceria nanoparticles for pro-oxidation of hydrogen peroxide, *Nano Res.*, 2020, **13**, 2384–2392.
21 M. Mogensen, Physical, chemical and electrochemical properties of pure and doped ceria, *Solid State Ionics*, 2000, **129**, 63–94.
22 A. Solovyev, A. Shipilova, E. Smolyanskiy, S. Rabotkin and V. Semenov, The Properties of Intermediate-Temperature Solid Oxide Fuel Cells with Thin Film Gadolinium-Doped Ceria Electrolyte, *Membranes*, 2022, **12**, 896.
23 A. Aguadero, L. Fawcett, S. Taub, R. Woolley, K.-T. Wu, N. Xu, J. A. Kilner and S. J. Skinner, Materials development for intermediate-temperature solid oxide electrochemical devices, *J. Mater. Sci.*, 2012, **47**, 3925–3948.
24 T. S. Hofer, F. M. Kilchert and B. A. Tanjung, An effective partial charge model for bulk and surface properties of cubic ZrO_2, Y_2O_3 and yttrium-stabilised zirconia, *Phys. Chem. Chem. Phys.*, 2019, **21**, 25635–25648.
25 D. S. Gunn, J. A. Purton and S. Metz, Monte Carlo simulations of gadolinium doped ceria surfaces, *Solid State Ionics*, 2018, **324**, 128–137.
26 H. Inaba, Molecular dynamics simulation of gadolinia-doped ceria, *Solid State Ionics*, 1999, **122**, 95–103.
27 F. Ye, T. Mori, D. R. Ou and A. N. Cormack, Dopant type dependency of domain development in rare-earth-doped ceria: An explanation by computer simulation of defect clusters, *Solid State Ionics*, 2009, **180**, 1127–1132.
28 M. J. Wiedemair and T. S. Hofer, Towards a dissociative SPC-like water model – probing the impact of intramolecular Coulombic contributions, *Phys. Chem. Chem. Phys.*, 2017, **19**, 31910–31920.
29 T. S. Hofer and M. J. Wiedemair, Towards a dissociative SPC-like water model II. The impact of Lennard-Jones and Buckingham non-coulombic forces, *Phys. Chem. Chem. Phys.*, 2018, **20**, 28523–28534.
30 T. S. Mahadevan and S. H. Garofalini, Dissociative Chemisorption of Water onto Silica Surfaces and Formation of Hydronium Ions, *J. Phys. Chem. C*, 2008, **112**, 1507–1515.
31 T. S. Mahadevan and S. H. Garofalini, Dissociative Water Potential for Molecular Dynamics Simulations, *J. Phys. Chem. B*, 2007, **111**, 8919–8927.
32 T. P. Senftle, S. Hong, M. M. Islam, S. B. Kylasa, Y. Zheng, Y. K. Shin, C. Junkermeier, R. Engel-Herbert, M. J. Janik, H. M. Aktulga, T. Verstraelen, A. Grama and A. C. T. van Duin, The ReaxFF reactive force-field: development, applications and future directions, *npj Comput. Mater.*, 2016, **2**, 15011.
33 R. V. Krishnan, G. Panneerselvam, P. Manikandan, M. Antony and K. Nagarajan, Heat Capacity and Thermal Expansion of Uranium-Gadolinium Mixed Oxides, *J. Nucl. Radiochem. Sci.*, 2009, **10**, 19–26.
34 S. Sameshima, M. Kawaminami and Y. Hirata, Thermal Expansion of Rare-Earth-Doped Ceria Ceramics, *J. Ceram. Soc. Jpn.*, 2002, **110**, 597–600.
35 M. Allen and D. Tildesley, *Computer Simulation of Liquids*, Oxford University Press, London, 2017.

36 J. W. Ochterski, *Vibrational analysis in Gaussian*, Gaussian, 1999, **http://gaussian.com/vib/**.
37 J. M. Gallmetzer and J. Gamper, *VibrationalAnalysis.jl.*, 2024, **https://github.com/MolarVerse/VibrationalAnalysis.jl**.
38 W. C. Swope, H. C. Andersen, P. H. Berens and K. R. Wilson, A computer simulation method for the calculation of equilibrium constants for the formation of physical clusters of molecules: Application to small water clusters, *J. Chem. Phys.*, 1982, **76**, 637–649.
39 H. J. C. Berendsen, J. P. M. Postma, W. F. van Gunsteren, A. DiNola and J. R. Haak, Molecular dynamics with coupling to an external bath, *J. Chem. Phys.*, 1984, **81**, 3684–3690.
40 D. Wolf, P. Keblinski, S. R. Phillpot and J. Eggebrecht, Exact method for the simulation of Coulombic systems by spherically truncated, pairwise r-1 summation. The, *J. Chem. Phys.*, 1999, **110**, 8254–8282.
41 A. Vaitkus, A. Merkys and S. Gražulis, Validation of the Crystallography Open Database using the Crystallographic Information Framework, *J. Appl. Crystallogr.*, 2021, **54**, 661–672.
42 M. Quirós, S. Gražulis, S. Girdzijauskaitė, A. Merkys and A. Vaitkus, Using SMILES strings for the description of chemical connectivity in the Crystallography Open Database, *J. Cheminf.*, 2018, **10**, 23.
43 A. Merkys, A. Vaitkus, J. Butkus, M. Okulič-Kazarinas, V. Kairys and S. Gražulis, COD::CIF::Parser: an error-correcting CIF parser for the Perl language, *J. Appl. Crystallogr.*, 2016, **49**, 292–301.
44 S. Gražulis, A. Merkys, A. Vaitkus and M. Okulič-Kazarinas, Computing stoichiometric molecular composition from crystal structures, *J. Appl. Crystallogr.*, 2015, **48**, 85–91.
45 S. Gražulis, A. Daškevič, A. Merkys, D. Chateigner, L. Lutterotti, M. Quirós, N. R. Serebryanaya, P. Moeck, R. T. Downs and A. L. Bail, Crystallography Open Database (COD): an open-access collection of crystal structures and platform for worldwide collaboration, *Nucleic Acids Res.*, 2011, **40**, D420–D427.
46 S. Gražulis, D. Chateigner, R. T. Downs, A. F. T. Yokochi, M. Quirós, L. Lutterotti, E. Manakova, J. Butkus, P. Moeck and A. L. Bail, Crystallography Open Database – an open-access collection of crystal structures, *J. Appl. Crystallogr.*, 2009, **42**, 726–729.
47 R. T. Downs and M. Hall-Wallace, The American Mineralogist Crystal Structure Database, *Am. Mineral.*, 2003, **88**, 247–250.
48 R. W. G. Wyckoff, *Crystal Structure*, Interscience Publishers, New York, 1963.
49 W. Zachariasen, The crystal structure of the modification C of the sesquioxides of the rare earth metals, and of indium and thallium, *Nor. Geol. Tidsskr.*, 1927, **9**, 310–316.
50 A. Erba, J. K. Desmarais, S. Casassa, B. Civalleri, L. Doná, I. J. Bush, B. Searle, L. Maschio, L. Edith-Daga, A. Cossard, C. Ribaldone, E. Ascrizzi, N. L. Marana, J.-P. Flament and B. Kirtman, CRYSTAL23: A Program for Computational Solid State Physics and Chemistry, *J. Chem. Theory Comput.*, 2022, **19**, 6891–6932.
51 L. Schimka, J. Harl and G. Kresse, Improved hybrid functional for solids: The HSEsol functional. The, *J. Chem. Phys.*, 2011, **134**, 024116.
52 J. P. Perdew, A. Ruzsinszky, G. I. Csonka, O. A. Vydrov, G. E. Scuseria, L. A. Constantin, X. Zhou and K. Burke, Restoring the Density-Gradient Expansion for Exchange in Solids and Surfaces, *Phys. Rev. Lett.*, 2008, **100**, 136406.
53 K. E. El-Kelany, C. Ravoux, J. K. Desmarais, P. Cortona, Y. Pan, J. S. Tse and A. Erba, Spin localization, magnetic ordering, and electronic properties of strongly correlated Ln_2O_3 sesquioxides (Ln = La, Ce, Pr, Nd), *Phys. Rev. B*, 2018, **97**, 245118.
54 J. K. Desmarais, A. Erba and R. Dovesi, Generalization of the periodic LCAO approach in the CRYSTAL code to g-type orbitals, *Theor. Chem. Acc.*, 2018, **137**, 28.
55 D. V. Oliveira, J. Laun, M. F. Peintinger and T. Bredow, BSSE-correction scheme for consistent Gaussian basis sets of double- and triple-zeta valence with polarization quality for solid-state calculations, *J. Comput. Chem.*, 2019, **40**, 2364–2376.
56 P. Manning, Oxygen self-diffusion and surface exchange studies of oxide electrolytes having the fluorite structure, *Solid State Ionics*, 1996, **93**, 125–132.
57 E. Ruiz-Trejo, Oxygen ion diffusivity, surface exchange and ionic conductivity in single crystal Gadolinia doped Ceria, *Solid State Ionics*, 1998, **113–115**, 565–569.
58 Y. Duan, C. Wu, S. Chowdhury, M. C. Lee, G. Xiong, W. Zhang, R. Yang, P. Cieplak, R. Luo, T. Lee, J. Caldwell, J. Wang and P. Kollman, A point-charge force field for molecular mechanics simulations of proteins based on condensed-phase quantum mechanical calculations, *J. Comput. Chem.*, 2003, **24**, 1999–2012.
59 B. R. Brooks, R. E. Bruccoleri, B. D. Olafson, D. J. States, S. Swaminathan and M. Karplus, CHARMM: A program for macromolecular energy, minimization, and dynamics calculations, *J. Comput. Chem.*, 1983, **4**, 187–217.